CHEMISTRY OF MATERIALS
Cite This: Chem. Mater. 2019, 31, 2731−2740
Article
pubs.acs.org/cm

Intrinsic Role of Cationic Substitution in Tuning Li/Ni Mixing in High-Ni Layered Oxides

Dawei Wang,[†,§,○] Chao Xin,[‡,○] Mingjian Zhang,[†,○] Jianming Bai,[∥] Jiaxin Zheng,[‡] Ronghui Kou,[⊥] Jun Young Peter Ko,[#] Ashfia Huq,[¶] Guiming Zhong,[§] Cheng-Jun Sun,[⊥] Yong Yang,[§] Zonghai Chen,[▽] Yinguo Xiao,[*,‡] Khalil Amine,[▽] Feng Pan,[*,‡] and Feng Wang[*,†]

[†]Sustainable Energy Technologies Department, and [∥]National Synchrotron Light Source II, Brookhaven National Laboratory, Upton, New York 11973, United States

[‡]School of Advanced Materials, Peking University, Peking University Shenzhen Graduate School, Shenzhen 518055, China

[§]Collaborative Innovation Center of Chemistry for Energy Materials, State Key Laboratory Physical Chemistry Solid Surfaces, Department of Chemistry, Xiamen University, Xiamen, Fujian 361005, China

[⊥]X-Ray Science Division, Advanced Photon Source, Argonne National Laboratory, Argonne, Illinois 60439, United States

[#]Cornell High Energy Synchrotron Source, Cornell University, Ithaca, New York 14853, United States

[¶]Chemical and Engineering Materials Division, Oak Ridge National Laboratory, Oak Ridge, Tennessee 37831, United States

[▽]Chemical Sciences and Engineering Division, Argonne National Laboratory, Argonne, Illinois 60439, United States

Supporting Information

ABSTRACT: Nickel-rich transition-metal (TM) layered oxides, particularly those with high Ni content, attract worldwide interest for potential use as high-capacity cathodes in next-generation Li-ion batteries. However, as Ni loading increases, Li and Ni sitting at octahedra tend to mix, resulting in reduced electrochemical activity, which has been one major obstacle to their practical applications. Herein, we investigate the kinetic and thermodynamic aspects of Li/Ni mixing in Li-$Ni_{0.7}Mn_xCo_{0.3-x}O_2$ ($0 \le x \le 0.3$) as they are synthesized, through quantitative determination of structural ordering and comparison to ab initio calculations. Results from this study elucidate the role of Co/Mn-substitution in tuning Li/Ni ordering, intrinsically through local magnetic interaction. Specifically, Co substitution facilitates Li/Ni ordering by relieving the intra-plane magnetic frustration and reducing the inter-plane super-exchange (SE) interaction; in contrast, Mn exacerbates magnetic frustration and strengthens SE, thereby aggravating Li/Ni mixing. These findings highlight the interplay between local magnetic interaction and cationic ordering, which has yet to be fully investigated for the needs of designing high-Ni layered cathodes and, broadly, TM-based oxides for various applications.

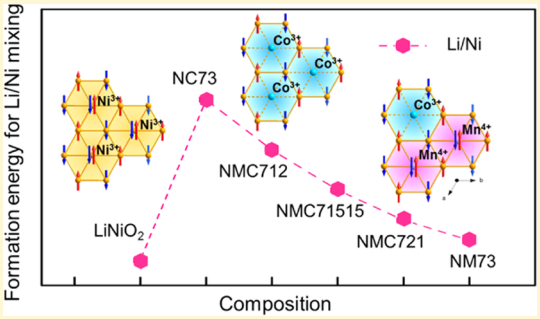

Transition metal (TM) oxides are naturally abundant and exhibit large varieties of structures and properties, and have found wide applications.[1] Notably, the multi-cation layered oxides, $LiNi_{1-x}(MnCo)_xO_2$ (generally called NMC), have been increasingly applied as high-capacity cathodes in lithium-ion batteries (LIBs). Among the NMC based cathodes, high-Ni ones are the most promising for near-future application in LIBs, particularly for transportation applications, because of their high specific capacities (180−220 mA h g^{-1}),[2−6] much higher than those of commercially available $LiCoO_2$ (140 mA h g^{-1}), $LiFePO_4$ (170 mA h g^{-1}), and $LiNi_{1/3}Co_{1/3}Mn_{1/3}O_2$ (160 mA h g^{-1}).[7,8] However, cationic disordering, generally shown as Li/Ni mixing in octahedral sites, becomes one big issue in this type of cathodes,[9−11] because it is detrimental to Li diffusivity, cycling stability, first-cycle efficiency, and overall electrode performance.[12−15] The recent studies through in situ probing synthesis process show that cationic ordering is highly coupled to the reconstruction of octahedra upon formation of the layered phase, and because of high diffusivity of Ni in the oxygen-deficient NiO_6 octahedra, serious Li/Ni mixing occurs.[16] In order to realize the full potential for commercial use, it is crucially important to tune Li/Ni ordering in high-Ni NMC during synthesis, but, on the other hand, it has been challenging because synthesis is such a complex process and often undertaken under non-equilibrium conditions. Therefore, not only the thermodynamics but also the kinetic aspects of the cationic ordering need to be taken into account in designing the synthesis of high-Ni NMC.[17−19]

Received: November 6, 2018
Revised: March 3, 2019
Published: March 7, 2019

DOI: 10.1021/acs.chemmater.8b04673
Chem. Mater. 2019, 31, 2731−2740

Thermodynamically, Li/Ni mixing has been mostly attributed to the propensity of Ni to form Ni^{2+}, the similar size of Ni^{2+} and Li^{+}, and the low energy barrier for the migration of Ni^{2+} ions.[20−24] According to these arguments, the Li/Ni mixing would prefer to take place in compounds with more Ni^{2+} ions. However, it contradicts the fact that high Li/Ni mixing has often been found in high-Ni layered NMC, wherein the population of Ni^{3+} ions is much higher than that of Ni^{2+}. Therefore, the unique structure and underneath interaction among constituent cations may play an important role in determining Li/Ni ordering. Particularly, super-exchange (SE) interaction should be considered since TM cations ($Ni^{2+/3+}$, Co^{4+}, Mn^{4+}) usually contain unpaired spin electrons.[25,26] In addition, those magnetic TM ions residing on the planes of edge-sharing equilateral triangles form an infinite triangular lattice. As a structural unit of two-dimensional (2D) triangular lattice, a single plaquette is composed of three TM spins. No matter how up and down spins are arranged, there is always at least one uncertain spin in the plaquette of triangular lattice, which can be considered a typical magnetic lattice with geometrical frustration, as illustrated in Scheme 1A. In such triangular frustrated lattices, the magnetic ordering is always suppressed because the competing interaction cannot be satisfied simultaneously.[27] Moreover, the instability of competing interaction might lead to nontrivial structure-related phenomena through the coupling with lattice degree of freedom for relief of magnetic frustration.[28−30]

Scheme 1. Illustration of This Study, through a Multimodal Approach Using in Situ, ex Situ Techniques and Ab Initio Calculations, to Determine the Relationship between the Kinetics, Thermodynamics of Cationic Ordering, and Local Magnetic Interaction in $LiNi_{0.7}Mn_xCo_{0.3-x}O_2$ ($0 \le x \le 0.3$). (A) In Situ Tracking of the Kinetic Proces of Cationic Ordering during Calcination (Left), Thermodynamics of Cationic Arrangement in the Intermediates and Final Products by ex Situ Studies (Middle), and the Magnetic Frustration and Super-Exchange (SE) by Theoretical Calculation (Right); (B) Given That the Fraction of Ni Is Fixed in a Series of Materials, 70% Ni in the Composition Leads to Two Ni Ions Occupying Two Corners of Triangular Lattice and the Third Corner Occupied by Magnetic Mn Ions and Non-Magnetic Co Ions, Allowing Systemic Studies of How Co/Mn Substitutions Impact the Cationic Ordering. Upon the Substitution of Co by Mn, the Spin Configuration Changes Accordingly, Representing the Increase in Magnetic Frustration and Thus the Increase in Li/Ni Mixing.

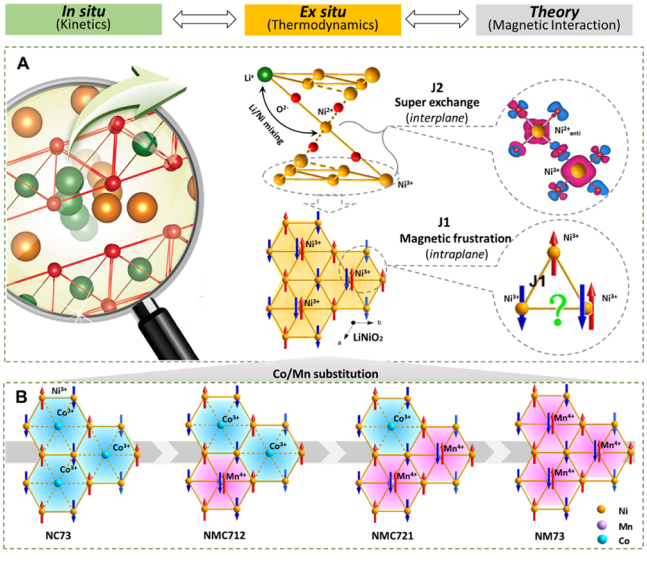

In this study, a multimodal approach is employed for determination of the kinetic synthesis process and related cationic ordering in preparing high-Ni $LiNi_{0.7}Mn_xCo_{0.3-x}O_2$ ($0 \le x \le 0.3$), via a combination of in situ synchrotron high-energy X-ray diffraction (HEXRD), absorption spectroscopy (XAS), neutron powder diffraction (NPD), and nuclear magnetic resonance (NMR). Quantitative analysis is made in order to identify the impact of Co/Mn substitution on the kinetics and thermodynamics of cationic ordering, and to make direct comparison to first-principles calculations. It is found that the presence of Co facilitates the Li/Ni ordering by reducing the strength of magnetic frustration and strengthening intra-plane SE interaction. Further substitution of Mn increases the strength of magnetic frustration and strengthens the inter-plane SE interaction, thereby aggravating Li/Ni mixing. These findings shed light on the intrinsic roles of Co/Mn in tuning Li/Ni mixing through local magnetic interaction, and so may help to pave the way for synthetic design of high-performance layered NMC cathodes and other TM-based functional materials.

Figure 1A shows the setup for in situ synchrotron HEXRD measurements of Li/Ni ordering/disordering in $LiNi_{0.7}Mn_xCo_{0.3-x}O_2$ ($0 \le x \le 0.3$) when subjected to high-temperature treatment. $LiNi_{0.7}Mn_{0.1}Co_{0.2}O_2$ (NMC712), $LiNi_{0.7}Mn_{0.2}Co_{0.1}O_2$ (NMC721), and $LiNi_{0.7}Mn_{0.3}O_2$ (NM73) were used in this study, wherein the concentration of Ni was fixed to occupy the two corners of frustrated triangular lattice, allowing to determine the effect of Co/Mn on Li/Ni disordering. Figure 1B shows the time-resolved HEXRD patterns recorded for NMC712 during heating at 850

DOI: 10.1021/acs.chemmater.8b04673
Chem. Mater. 2019, 31, 2731−2740

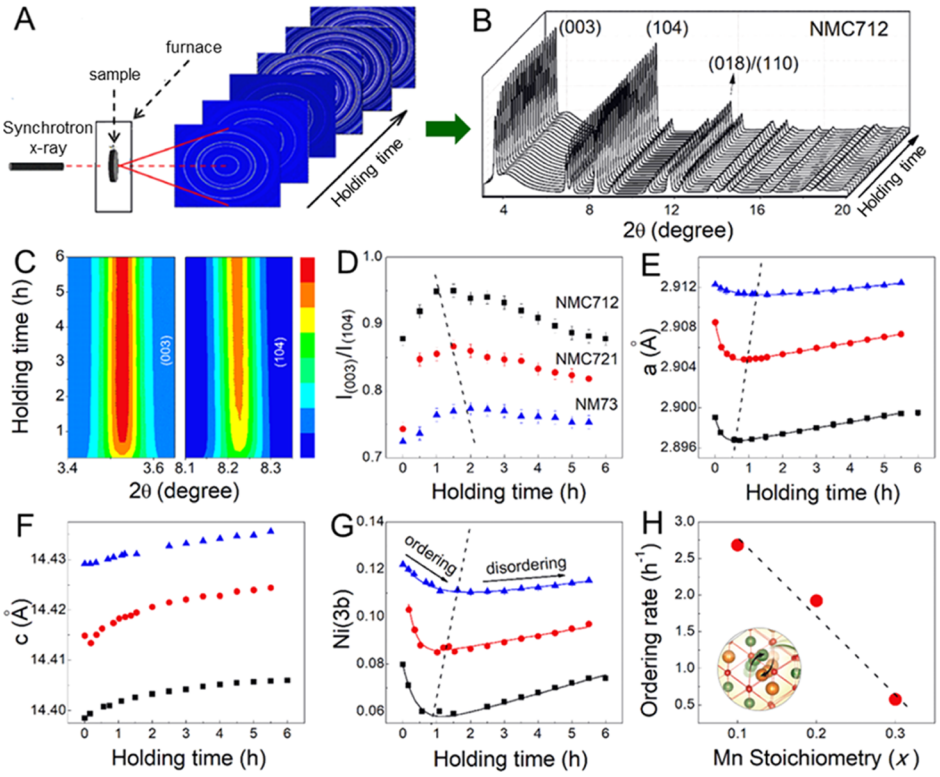

Figure 1. In situ tracking of cationic ordering/disordering in $LiNi_{0.7}Mn_xCo_{0.3-x}O_2$ ($0 \le x \le 0.3$) during calcination at 850 °C. (A) Schematic illustration of the experimental setup for in situ HEXRD measurements. (B) Time-resolved HEXRD patterns recorded at 850 °C during the synthesis of $LiNi_{0.7}Mn_{0.1}Co_{0.2}O_2$ (NMC712), with wavelength λ = 0.2953 Å. (C) Intensity maps of characteristic peaks (003), (104) in Figure 1B. (D−G) Evolution of the $I_{(003)}/I_{(104)}$ ratio, lattice parameter *a*, *c*, and occupancy of Ni at 3b sites, respectively, as a function of holding time for NMC712 (black square), NMC721(red circle), and NM73 (blue triangle). The solid lines in (E,G) represent the fitting of lattice parameter *a* and the anti-site occupancy of Ni at 3b sites, Ni(3b), as a function of time, by using an exponential-linear function $y = A_1\exp(-kt) + bt + y_0$; the error bars represent standard deviations derived from the Rietveld refinements. (H) Dependence of the kinetics of cationic ordering on Mn stoichiometry; see results from the quantitative analysis listed in Table 1.

°C. The layered structure was already formed at the very beginning of calcination because they had been pre-heated at 500 °C for 10 h.[17] The extension of holding time at 850 °C for up to 6 h led to initial improvement and then deterioration of Li/Ni ordering, as indicated by the evolution of peak intensity in (003) ($I_{(003)}$) and (104) ($I_{(104)}$) reflections. Similar behaviors were also observed in NMC721 and NM73 (Figure S1).

Because Li/Ni mixing has negligible impact on $I_{(104)}$ but significant impact to $I_{(003)}$, the $I_{(003)}/I_{(104)}$ ratio is usually used to evaluate the degree of Li/Ni mixing.[9] As shown in Figures 1C and S2, $I_{(104)}$ for NMC712, NMC721, and NM73 increased slightly in the first 2 h of holding and then leveled off, whereas $I_{(003)}$ increased quickly and then decreased in all three samples. As a result, the $I_{(003)}/I_{(104)}$ ratio increased initially and then decreased continuously with holding (as demonstrated in Figure 1D), indicating the competition between ordering/disordering processes during calcination. Li NMR was carried out to identify the site occupancy and local environment of Li because X-ray is not sensitive to light element Li. As will be discussed below (in Figures S3 and 2A), both ^{6}Li and ^{7}Li NMR spectra of the series of samples showed the presence of Li in TM(3a) in addition to Li(3b) sites. Thus, an anti-site model $(Li_{1-x}Ni_x)_{3b}(TM_{1-y}Li_y)_{3a}O_2$ was used for Rietveld refinement of individual HEXRD patterns from in situ measurements, to obtain quantitative information on the structural evolution. In this model, TM(3a) sites are randomly occupied by Ni, Mn, and Co with the designed stoichiometry, and the changes are only related to the concentration because of the solid solution nature of the layered structure. For the refinement, pure layered structure ($R\bar{3}m$) was used as the model because fitting using the other models, such as spinel structure ($Fd\bar{3}m$) and mixing phase (of layered structure and spinel structure), did not bring any further improvements (Figure S4).

Figure 1E−G present the quantitative structural evolution of NMC712, NMC721, and NM73 during calcination at 850 °C (detailed information from Rietveld refinement is given in Table S1). At the beginning of the holding, both lattice parameters *a* and occupancy of Ni^{2+} at 3b sites showed an exponential decay, indicating the fast Li/Ni ordering. After holding at 850 °C for a certain time (~1 h or longer), they reached minimum values and increased linearly thereafter, indicating Li/Ni disordering caused by Li/O loss at high temperatures. Li/Ni ordering and disordering occurred concomitantly throughout the calcination, with ordering being dominant at the beginning and then disordering becoming dominant after a long holding time (as a result of Li/O loss).[32] The c/a ratio, as another characteristic of Li/Ni ordering besides the $I_{(003)}/I_{(104)}$ ratio and anti-site Ni content, confirmed the trend of change during the calcination process (Figure S5).

As shown in Figure 1G, it took longer time for the occupancy of Ni(3b) to reach the minimum with the increase

DOI: 10.1021/acs.chemmater.8b04673
Chem. Mater. 2019, 31, 2731−2740

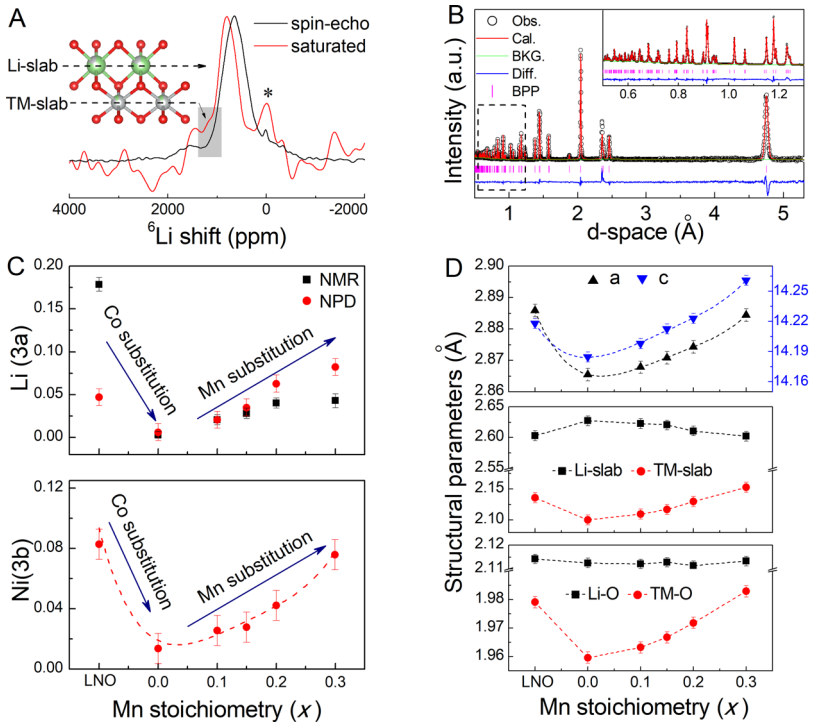

Figure 2. Thermodynamic impact of Co/Mn substitution on the structural ordering in $LiNi_{0.7}Mn_xCo_{0.3-x}O_2$ ($0 \le x \le 0.3$). (A) ^{6}Li NMR spectra for identifying the Li occupancy in the Li-slab (3b sites) and TM-slab (3a sites) in the synthesized NM73, by spin-echo sequence and reversion recovery sequence (saturated) with recovery time of 0.012 s (see also Figure S3 for other compositions without applying the reversion recovery sequence). The peak at about 4 ppm (labeled by "*") comes from Li_2CO_3/LiOH, whereas other unmarked peaks are attributed to the side bands and background. (B) NPD patterns of NM73 in comparison to the calculated patterns by Rietveld refinement. In the plots, black dots: observed data; red lines: calculated data; purple bars: Bragg peak positions, blue lines: difference between the observed and calculated data; green lines: background. (C) Anti-site occupancy of Li at 3a sites and Ni at 3b sites, with strong dependence on Co and Mn stoichiometry. (D) Lattice parameters a (black triangle) and c (blue triangle), Li/TM-slab distances, and bond lengths from refinements of the NPD data, showing strong dependence on Co and Mn stoichiometry. The error bars in (C, D) represent standard deviations obtained from Rietveld refinements.

Table 1. Parameters Obtained from Fitting to the Time Dependence of Lattice Parameter a and Cationic Disordering [i.e. Ni at 3b Sites; Ni(3b)] Using the Equation $y = A_1 \exp(-kt) + bt + y_0$.

composition	lattice parameter a				anti-site occupancy Ni(3b)			
	A_1	k	b	y_0	A_1	k	b	y_0
NMC712	0.0028(1)	4.869(1)	0.00059(1)	2.896(1)	0.0289(1)	2.684(1)	0.00421(1)	0.063(1)
NMC721	0.0043(1)	4.491(1)	0.00057(1)	2.904(1)	0.0329(1)	1.924(1)	0.00276(1)	0.099(1)
NM73	0.0017(1)	1.271(1)	0.00035(1)	2.910(1)	0.0277(1)	0.576(1)	0.00343(1)	0.122(1)

in Mn content, which indicates that the Mn content greatly affected the kinetics of Li/Ni ordering in NMC. Therefore, in order to quantify the ordering kinetics, we used $y = A_1 \exp(-kt) + bt + y_0$ (a combination of exponential and linear functions) to fit the evolution of the lattice parameter a and anti-site occupancy (of Ni^{2+} at 3b sites) with time (see detailed discussion in the Supporting Information, Section S1).[17,33] Herein, parameters k and b represent the kinetics of Li/Ni ordering and disordering, respectively. From the fitting (as shown in Figure 1H and Table 1), it is clear that k decreased obviously with increasing Mn content, whereas b decreased a bit, confirming the role of Mn substitution in slowing down both Li/Ni ordering and disordering, especially the Li/Ni ordering process. More obvious behavior was observed in preparing NMC71515, wherein Li/Ni ordering took over throughout the calcination process, in contrast to the behavior observed in the non-Mn-containing counterpart, NC73, where serious Li/Ni disordering occurred after 850 °C (Figure S6 and Section S2). As shown in Figure 1G, the lowest Li/Ni mixing was reached in the sample calcined at 850 °C for ~2 h, giving arise to reasonably good electrochemical performance (Figure S7).[17] In short, Mn substitution not only slowed down the kinetics of Li/Ni ordering but also aggravated the degree of Li/Ni mixing.

With insights from the in situ studies, we prepared a series of NMC materials (of varying Co/Mn content), with the Li/Ni mixing minimized in order to get close to their thermodynamic state. Five samples, LNO, NC73, NMC712, NMC721, and NM73, were synthesized and then characterized by NMR and NPD. Li NMR is sensitive to local environment around Li (as shown in Figure S3). Only two peaks were observed in $^{6/7}$Li NMR spectra: the overlapped Li signal in layered phase and Li_2CO_3/LiOH at around 300−1200 and ~4 ppm, respectively. By means of the difference in relaxation time (T_1) of Li at 3a and 3b sites, a recovery pulse was applied to saturate Li at 3b site and suppress its signal, in order to highlight Li at the TM site. By doing this, a small shoulder peak was directly observed at the low field side (~1260 ppm) for NM73, confirming the existence of Li at TM(3a) sites in high-Ni layered oxides, although the amount is small (see Figure 2A,

DOI: 10.1021/acs.chemmater.8b04673
Chem. Mater. 2019, 31, 2731−2740

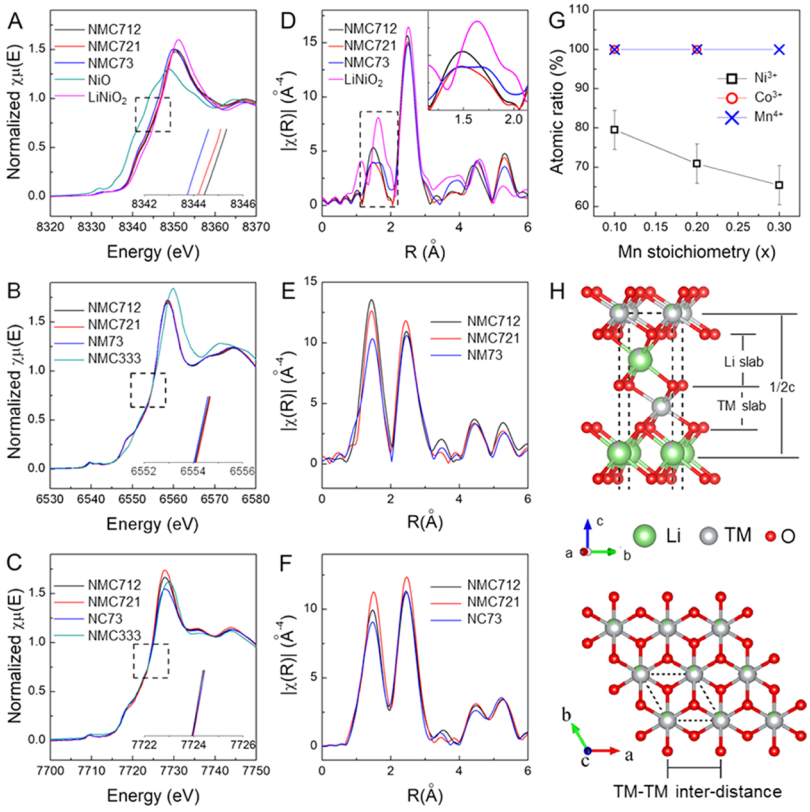

Figure 3. Valence state and local environment of Ni, Mn, Co in $LiNi_{0.7}Mn_xCo_{0.3-x}O_2$ ($0 \le x \le 0.3$). (A−C) X-ray absorption near-edge structure for Ni, Mn, and Co K-edges, respectively (inset: zoom-in view in the selected energy ranges at half-maximum magnitude of the peaks). (D−F) Fourier transform (FT) of the extended X-ray absorption fine structure for Ni, Mn, and Co K-edges, respectively. (G) Atomic percentage of fully oxidized TM ions (i.e., Ni^{3+}, Co^{3+}, and Mn^{4+}), the error bars represent standard deviations obtained from spectral fittings. (H) Illustration of the layered structure and relevant bond length: $0.5c = 1.5\ (d_{\text{Li-slab}} + d_{\text{TM-slab}})$, and the value of a equals to TM−TM inter-distance ($d_{\text{TM-TM}}$).

Section S3).[34] ^{7}Li peak of NC73 shifted to the high-field side compared to LNO, indicating the higher shielding from neighboring atoms and the shorter distance. With the further substitution of Co by Mn, ^{7}Li peak shifts to the low-field side, indicating the low screening from neighboring atoms and the expansion of local environment. High-resolution ^{6}Li NMR was measured from the obtained samples, in order to clarify and differentiate the Li in the Li-slab and TM-slab (Figure S3). The quantitative analysis by fitting ^{6}Li NMR spectra indicated that NC73 had the lowest Li content at TM(3a) sites, whereas it increased with the substitution of Mn (Figures 2C and S3, Table S2).

Rietveld refinement was made to the NPD data by using the same model and constraint as used for the HEXRD data (Figures 2B and S8). The main results are given in Figure 2C,D and Table S3. Within the composition range tested, the plots of lattice parameters (a and c) and anti-site occupancy (of Ni^{2+} at 3b sites, and of Li at 3a sites) as a function of Mn concentration show an upside-down parabola-like shape, similar to the Li occupancy at 3a sites from NMR (Figure 2C). NC73 showed the smallest values in the lattice parameters a and c, as well as in the occupancy of Ni^{2+} at 3b sites and of Li^+ at 3a sites, indicating that Co substitution led to the decrease in lattice parameters and suppression of Li/Ni mixing; in contrast, further replacement of Co by Mn caused the gradual increase in both lattice parameters and Li/Ni mixing. In the whole series, NC73 shows the largest Li-slab distance, indicating the best ionic conductivity and rate performance among the compositions (Figure 2D).[12] Overall, NMR results and NPD data agreed well with each other although the values are slightly different because of the difference in their sensitivity to Li. From these two complementary experiments, we demonstrated that the substitution of Co by Mn increased the lattice parameters a and c and the anti-site Li at TM(3a) sites and anti-site Ni at Li(3b) sites. In addition, the composition calculated from the Rietveld refinement is quite close to the designed stoichiometry (Table S3), indicating that the stoichiometry is well controlled during the calcination process.

Intriguingly, TM−O bond length showed a similar upside-down parabola, whereas the Li−O bond length showed negligible change (Figure 2D), which may be related to the valence states of the TMs. X-ray absorption near-edge spectroscopy (XANES) was used to examine the valence states of individual elements (Ni, Mn, and Co) and their local environment (Figure 3). With the increase in Mn content, the edge of Ni K-edge spectra shifted to lower energies, indicating that the average valence state of Ni decreased, in contrast to the minor change in the XANES of the Co and Mn K-edges (Figure 3A−C). Herein, Mn K-edge spectrum from NMC333 is used here as a reference for Mn(IV).[35] Valence states of TMs in different compositions were further quantified by linear fitting of XANES spectra using standard references (Figure S9). As demonstrated in Figure 3G, with the increase in Mn content from 0.1 to 0.3, the fraction of Ni^{3+} decreased, from ~79 to 65%, whereas the fraction of Co^{3+} and Mn^{4+} remained nearly constant, at around 1.0. Consequently, with the replacement of Co^{3+} by Mn^{4+}, more Ni^{2+} was introduced

DOI: 10.1021/acs.chemmater.8b04673
Chem. Mater. 2019, 31, 2731−2740

into the system for charge compensation. Moreover, compared to NC73, an extra 10, 20, and 30% Ni^{2+} should be expected to compensate for the charge balance of Mn^{4+} substitution in NMC712, NMC721, and NM73. However, the anti-site Ni^{2+} was increased only from 1.36 to 2.56, 4.23, and 7.57%, respectively (as calculated from NPD refinement), much smaller than those of newly introduced Ni^{2+}. This finding means that most of the newly introduced Ni^{2+} is located at the 3a sites of the TM-slab rather than the 3b sites of the Li-slab, and so it did not cause much change to the Li−O bond length, but significant change to the TM−O bond length (as shown in Figure 2D).

Fourier transform (FT) of EXAFS spectra was carried out to characterize the local bond length of individual TMs (Figure 3D−F; see also Figure S10 for the high-quality XAS data in k space). Some more details about the fitting and related results of Ni K-edge EXAFS are provided in Section S4, Figure S11, and Table S4. With the increase in Mn content, the bond lengths of both Mn−O and Co−O show negligible change (both around 1.4 Å), corresponding to the constant valence state of Mn(4+) and Co(3+). However, the peak associated with Ni−O bond exhibits obvious change with the introduction of Mn: a shoulder peak at 1.7 Å was observed and became more obvious as the Mn content increased. The peaks at 1.5 and 1.7 Å correspond to Ni^{3+}−O and Ni^{2+}−O bond length, respectively. As the population of Ni^{2+} increased with the Mn content, the height of shoulder peak at 1.7 Å increased (see also Table S4), which agrees with the NPD results. There is a small fluctuation in the peak intensity of the FT-EXAFS data likely because of the change in the relative concentration of Ni^{2+}/Ni^{3+} (Figure 3D). The Jahn-Teller effect is well demonstrated in the FT-EXAFS of the reference LNO, as shown by the obvious peak splitting, with features both at ∼1.65 Å, and at 2.0 Å (Figure 3D), similar to the observation in early studies.[20,36] However, in the presence of Mn, the effect becomes more complex and is not well followed in NMC712, NMC721, and NM73, similar to observations in other NMC-based complex systems.[31,37−40]

As schematically illustrated in Figure 3H (for half-unit cell), the lattice parameters a and c highly depend on the size of TMO_6 and LiO_6 octahedrons, specifically, $0.5c = 1.5d_{\text{Li-slab}} + 1.5d_{\text{TM-slab}}$, and a equals the TM−TM inter-distance ($d_{\text{TM−TM}}$), which are eventually determined by bond length. The $d_{\text{Li-slab}}$ and $d_{\text{TM-slab}}$ are presented in Figure 2D, the $d_{\text{TM-slab}}$ shows a same trend with the lattice parameters a and c, whereas $d_{\text{Li-slab}}$ shows a reverse trend, indicating the lattice parameters are determined by $d_{\text{TM-slab}}$ and TM−O bond length. The bond length is determined by the valence state of Ni and its distribution (disordering). The valence state of Ni decreased with the introduction of Mn, thereby causing increase in the average bond length of TM−O and $d_{\text{TM-slab}}$. Overall, the change in Li/Ni mixing did not cause much change in the Li−O bond length or $d_{\text{Li-slab}}$ (as shown in Table S3). From both NPD and XAS data, the composition dependence of macroscopic lattice parameters (such as a, c, Li−O bond length, and average TM−O bond length) is determined.

By studying the cationic ordering in the pure LNO and a series of $LiNi_{0.7}Mn_xCo_{0.3-x}O_2$, we were able to show the important role of Mn/Co substitution in tuning the Li/Ni mixing. Simply put, Co substitution facilitates Li/Ni ordering, whereas Mn substitution makes it worse, which, however, may not be explained by the change of ionic radius as traditionally believed.[21−24] First of all, in the case of pure LNO, despite the high concentration of Ni^{3+}, the Li/Ni mixing is higher than any other Mn/Co-substituted variants (as shown in Figures 2 and 3). Here, through quantitative determination of the structural ordering from multimodal characterization, we may have better understanding of the impact of Mn/Co substitution on Li/Ni mixing. As given in Table S5, the evolution of lattice parameter a as a function of Mn/Co substitution is expected to increase from 1 to 1.050 (normalized to NC73), as the Mn content increased from 0 to 0.3 when estimated only from the ionic radius; it is much different than experimental results, which is from 1 to 1.007 when normalized to NC73 (Table S3). The large discrepancy indicates that, in addition to the effect of ionic radius, other effects, such as electrostatic and magnetic interaction (as illustrated in Scheme 1), may play an important role. In the layered structure, the charge state is neutral and so the effects of their local distribution caused by Mn/Co substitution should be negligible to the macro-crystal lattice. Typically, magnetic frustration exists in a 2D triangular lattice with the magnetic Ni^{2+} and Ni^{3+} ions, and inevitably destabilizes the crystal structure, which should play a key role in determining the crystal structure. The appearance of non-magnetic Li^+ in the TM layer will relieve magnetic frustration through removal of competing magnetic interaction on the neighbor site and, therefore, stabilize the crystal structure (Scheme 1). On the other hand, the appearance of magnetic Ni_{anti}^{2+} in the Li^+ layer will also relieve magnetic frustration through the provision of magnetic SE interaction between spin of Ni^{2+} and spins of TM ion in TM-slab bridged by O ions. Hence, the occurrence of Li/Ni mixing is beneficial to the stabilization of the layered crystal structure of NMC through relief of magnetic frustration, which is the origin of Li/Ni mixing from the view of thermodynamics. If magnetic $Ni^{2+/3+}$ ions are replaced by non-magnetic Co^{3+} ions in a low-spin state, the magnetic frustration can be relieved and the crystal structure can be stabilized with less Li/Ni disordering. That is why NC73 has the lowest Li/Ni mixing in the series. As Mn^{4+} substitutes Co^{3+}, the spins of magnetic Mn^{4+} ions will enhance the magnetic frustration of triangular lattice (Scheme 1); thus, Li/Ni mixing is aggravated in order to release the frustration and stabilize the crystal structure.

In order to quantify the effects of cationic substitution on Li/Ni mixing, we carried out ab initio calculations based on the GGA + U approach (see Section S5). First, these calculations were performed for LNO based on the anti-site Li/Ni model along with the consideration of the ferromagnetic (FM) and anti-FM (AFM) structure. A value close to the NPD result, 10% of the Li/Ni anti-site defect, was chosen for the calculations. The spin density of states (sDOS) of LNO with FM and AFM magnetic structure are plotted in Figures S12 and S13, and it can be seen that LNO with AFM magnetic structure shows a semiconductor characteristic with a band gap. In addition, the system with lowest energy manifested a preference for the space group C2/m with G-type anti-FM ordering (G-AFM; see detailed discussion in the Supporting Information, Section S7 and Table S6). For simplification, the Li/Ni defect of 10% and space group of C2/m with G-AFM were applied to all cathode compositions.

The calculated lattice parameters a and c are shown in Figure 4A and Table S7. The calculated values are slightly higher than the experimental data, mostly because of using a larger value of the Li/Ni mixing for the calculations. Importantly, it can be seen that from NC73 to NM73, the lattice a increased from 1 to 1.021 (normalized to NC73)

DOI: 10.1021/acs.chemmater.8b04673
Chem. Mater. 2019, 31, 2731−2740

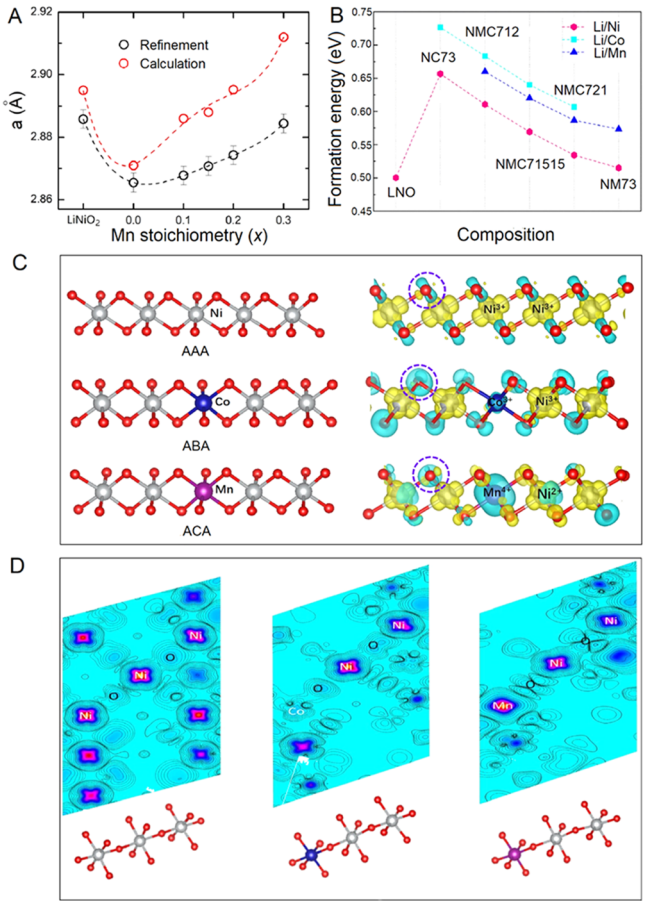

Figure 4. Electronic structure for LNO and $LiNi_{0.7}Mn_xCo_{0.3-x}O_2$ ($0 \le x \le 0.3$) revealed by theoretical calculations. (A) Lattice parameter *a*, from refinement of NPD data (black open circles), in comparison to calculated values in the presence of Li/Ni mixing (red open circles). (B) Calculated formation energy (E_f) for Li/TM anti-site defects (with the content of 10%). (C) 3D spin electron density contour maps along the [001] plane to illustrate the intra-plane SE interactions. (D) 2D charge density contour maps along the plane of TM−O−Ni 180° directions in LNO (left), NC73 (middle), and NM73 (right).

when considering the magnetic interactions (including magnetic frustration and SE), which is much close to the experimental value than that estimated only from the ionic radius. This indicates that the magnetic interactions, rather than the ionic radius caused by Mn/Co substitution, play an important role in determining the lattice parameters and Li/Ni mixing. Figure 4B shows the calculated average formation energy (E_f) of the Li/Ni anti-site defect in $LiNi_{0.7}Mn_xCo_{0.3-x}O_2$ ($0 \le x \le 0.3$) (The formation energy was defined in the Supporting Information, Section S8). The anti-site Li/Ni in LNO has the smallest E_f, only ~500 meV, indicating that Li/Ni mixing happens readily; once Co is introduced (as in NC73), the value of E_f is greatly increased, indicating that the Co substitution makes Li/Ni mixing more difficult, a finding that is consistent with experimental observations.[32,41] With the introduction and further increase of Mn content, E_f gradually decreased, indicating that the possibility of Li/Ni mixing would increase. These calculated results are consistent with the experimental results (Figure 2C). The E_f of Li/Co and the Li/Mn anti-site were also calculated (Figure 4B), and they show much larger values than those of Li/Ni mixing, indicating that Li/Co and Li/Mn mixing are not likely to happen from the viewpoint of thermodynamics.[41] In contrast, results from calculations ignoring the spin polarization of Ni, Co, and Mn ions (as presented in Figures S14 and S15), are chaotic and not consistent with the experimental results, indicating that the spin polarization plays an indispensable role in Li/Ni mixing in the NMC systems. Such an inconsistency is mainly because the single-point energy of NMC without spin polarization is not the ground-state energy. In addition, the intensities of SE interactions between different TMs are also neglected, which directly affect the calculated formation energies. Thus, the impact of SE interactions on cationic disordering should be further analyzed.

The spin density corresponding to the structure unit is plotted in Figure 4C. This stability of structure unit was decided by electronic SE. A class of inorganic supramolecular chains is formed in space. In pristine LNO, FM SE interaction within the TM-slab is mediated via the oxygen anion by forming a 90° Ni−O−Ni bond, shown in Figure S15B, which is weak according to the Goodenough−Kanamori−Anderson rules.[42] Both Ni^{2+} ($t_{2g}^6e_g^2$) and Ni^{3+} ($t_{2g}^6e_g^1$) have fully occupied t_{2g} states and partially filled e_g states (Figures S16D and S17). As shown in Figure S18 (for comparison with the sDOS), 180° Ni_{anti}−O−Ni inter-plane SE should be stronger than the 90° Ni−O−Ni intra-plane SE because of the more occupied states below the Fermi level. The O anion between the spin parallel Ni forms a σ-bond, and the O anion between the spin anti−parallel Ni_{anti}^{2+} forms a π-bond (as illustrated in Figure S19). This 180° Ni_{anti}−O−Ni SE interaction lowered the whole system energy, thereby stabilizing Ni_{anti}^{2+} in the Li-slab. From the above, we deduced that 180° inter-plane Ni_{anti}−O−Ni SE interaction is favorable for forming anti-site Li/Ni defects.

However, introduction of Co can decrease magnetic frustration, enhance the intra-plane 90° Ni−O−Ni SE interaction, and screen the inter-plane 180° Ni_{anti}−O−Co interaction, which may explain the decrease of Li/Ni mixing by substitution of Ni with Co.[32,41,43] (see Section S9 and Figure 2C,D). Further replacement of Co with Mn aggravated Li/Ni mixing, as suggested by the reduction of E_f with the increase in Mn content (Figure 4B), which may be in part because of the introduction of extra Ni^{2+} neighboring Mn cations to increase magnetic frustration (for charge compensation, see Figure 3G). In addition, SE interaction may also play an important role in causing Li/Ni mixing. As shown in Figure 4C (bottom), the t_{2g} orbital of Mn^{4+} will interact with the p orbital of the O anion to form a strong π bond, leading to weak 90° Mn−O−Ni interaction in the TM layer. In the meanwhile, there will be inter-plane 180° Ni_{anti}^{2+}−O^{2-}−Mn^{4+} SE interaction (Figure 4D, right), which is much stronger than inter-plane Ni_{anti}^{2+}−O^{2-}−Co^{3+} interaction (Figure 4D, middle).

The 90° and 180° SE interactions in $LiNi_{0.7}Mn_{0.3}O_2$ were also depicted by 3D spin electron density maps (Figure S20). Unlike direct interaction, SE interaction needs the O ion as a carrier, and its strength is reflected by the spin density of the O ion. The irrelative strengths are summarized in Figures S20 and S21 and Table S8. Overall, the weaker intra-plane 90° Mn−O−Ni SE interaction and the stronger inter-plane 180° Ni_{anti}−O−Mn SE interaction compared with Ni_{anti}−O−Co interaction favor the reduction of the E_f of the Li/Ni anti-site, stabilizing the anti-site Ni_{anti}^{2+} and aggravating Li/Ni mixing. It

DOI: 10.1021/acs.chemmater.8b04673
Chem. Mater. 2019, 31, 2731−2740

also can be found that 90° Ni−O−Ni SE interaction is weak, whereas 180° Ni−O−Ni SE interaction is strong.

As illustrated in Scheme 1, the Li/Ni ordering involves the Ni^{2+} migration at octahedral sites (i.e., between Li(3b) sites to TM(3a) sites), and therefore, the ordering kinetics is determined by the activation energy for Ni^{2+} migration from Li (3b) sites to TM (3a) sites, eventually, by the local interaction, notably inter-plane SE and intra-plane magnetic interactions. Theoretical calculation revealed that Co substitution released the magnetic frustration in TM-slab and weakened the 180° Ni−O−TM SE, decreased the repulsion force to Ni^{2+} in TM-slab, and destabilized the Ni^{2+} in Li-slab. Therefore, Co substitution reduced the activation energy required for Ni^{2+} migration from Li (3b) sites to TM (3a) sites, therefore increasing the Li/Ni ordering kinetics (Figure 1E−H). In contrast, Mn substitution increased the magnetic frustration in the TM-slab and strengthened the 180° SE, increased the repulsion force to Ni^{2+} in the TM-slab, and stabilized the Ni^{2+} in the Li-slab. Therefore, Mn substitution increased the activation energy for Ni^{2+} migration from Li-slab to TM-slab, and decreased the kinetics of Li/Ni ordering during calcination process (Figure 1E−H).

By using the developed approach, we have also extended the study to the Cr^{3+}-substituted $LiCr_xNi_{1-x}O_2$ system. In $LiCr_xNi_{1-x}O_2$, the magnetic Cr^{3+} with $S = 3/2$ will replace not only Ni^{3+} with $S = 3/2$ but also Ni^{4+} with $S = 2$, resulting in the diminishing of magnetic frustration. Through calculation of the inter- and intra-plane magnetic interactions in the $LiCr_xNi_{1-x}O_2$ system (Section 10, Figure S22), we found that the 180° Ni^{2+}−O−Cr^{3+} SE is weaker than the 180° Ni−O−Ni SE (Figure S23). In addition, because of the compensation of the charge, Cr^{4+} will form with the increase in Cr content. However, Cr^{4+} could not form 180° SE with anti-site Ni^{2+} (Figure S23). Therefore, the Cr substitution reduced the average 180° Ni−O−TM SE in $LiCr_xNi_{1-x}O_2$ system. Briefly speaking, the substitution of Ni by Cr diminished the magnetic frustration and reduced the 180° Ni−O−TM SE, thus decreasing the Li/Ni mixing in $LiCr_xNi_{1-x}O_2$, which is in agreement with the experimental results.[44] This, again, validates the developed approach in this work that allows explaining the intrinsic role of substitution, of not only Co/Mn but Cr and potentially other TMs.

In summary, a combination of in situ, ex situ experimental and theoretical studies revealed the relationship between the cationic ordering (both kinetics and thermodynamics) and magnetic interactions (including intra-plane magnetic frustration and inter-plane SE) in the high-Ni $LiNi_{0.7}Mn_xCo_{0.3-x}O_2$ ($0 \le x \le 0.3$) system. Co substitution in 3a sites diminishes the inter-plane 180° Ni_{anti}−O−Ni SE interaction and relieves the intra-plane magnetic frustration, thereby reducing the activation energy for Ni^{2+} migration from Li(3b) sites to TM(3a) sites, which eventually leads to the increase in the kinetics of cationic ordering, and low Li/Ni mixing in the final phase. Further substitution of Mn for Co in 3a sites not only introduces extra Ni^{2+} but also enhances the intra-plane magnetic frustration, and provides stronger inter-plane 180° Ni_{anti}−O−Mn SE interaction, thus increasing the activation energy for Ni^{2+} migration from Li(3b) sties to TM(3a) sites, reducing the ordering kinetics and aggravating final Li/Ni ordering. This study demonstrated, for the first time, the crucial role of magnetic frustration and SE interactions in determining the local structural ordering of TM oxides, hence offering new insights into the synthetic design of high-Ni cathodes for LIBs and, broadly, TM-based materials for various applications.

■ ASSOCIATED CONTENT

Supporting Information

The Supporting Information is available free of charge on the ACS Publications website at DOI: 10.1021/acs.chemmater.8b04673.

Experimental sections; in situ HEXRD; ex situ NMR; ex situ NPD; ex situ XAS; calculations (PDF)

■ AUTHOR INFORMATION

Corresponding Authors

*E-mail: xiaoyg@pkusz.edu.cn (Y.X.).
*E-mail: panfeng@pkusz.edu.cn (F.P.).
*E-mail: fwang@bnl.gov (F.W.).

ORCID

Zonghai Chen: 0000-0001-5371-9463
Khalil Amine: 0000-0001-9206-3719
Feng Pan: 0000-0002-8216-1339
Feng Wang: 0000-0003-4068-9212

Author Contributions

○D.W. C.X. and M.Z. contributed equally.

Notes

The authors declare no competing financial interest.

■ ACKNOWLEDGMENTS

We thank Yusuf Celebi, Eric Dooryhee, Sanjit Ghose, and John Trunk for technical support and Tiffany Bowman for graphic design. This work is partially supported by the U.S. Department of Energy (DOE) Office of Energy Efficiency and Renewable Energy, Vehicle Technology Office, contract no. DE-SC0012704. Synchrotron measurements conducted in the F2 beamline, at Cornell High Energy Synchrotron Source (CHESS), is supported by the National Science Foundation and the National Institutes of Health/National Institute of General Medical Sciences under NSF award DMR-1332208. Synchrotron measurements were conducted in the 28-ID-2 beamline of the National Synchrotron Light Source II, a U.S. Department of Energy (DOE) Office of Science User Facility operated for the DOE Office of Science by Brookhaven National Laboratory under contract no. DE-SC0012704. Neutron powder diffraction measurement at ORNL's Spallation Neutron Source was sponsored by the Scientific User Facilities Division, Office of Basic Energy Sciences, US Department of Energy. F.P. would like to acknowledge the National Materials Genome Project (2016YFB0700600), Guangdong Key-lab Project (no. 2017B0303010130), and Shenzhen Science and Technology Research grant (no. ZDSYS201707281026184). Y.Y. would like to acknowledge the National Natural Science Foundation of China (grant no. 21233004) for their research. Z.C., and K.A. would like to acknowledge the support of DOE to ANL. J.B. would like to acknowledge support of NSLS-II, a U.S. Department of Energy (DOE) Office of Science User Facility operated for the DOE Office of Science by Brookhaven National Laboratory, under contract no. DE-SC0012704. This research used resources of the Advanced Photon Source, an Office of Science User Facility operated for the U.S. Department of Energy (DOE) Office of Science by Argonne National Laboratory, and was supported by the U.S. DOE under contract no. DE-AC02-

DOI: 10.1021/acs.chemmater.8b04673
Chem. Mater. 2019, 31, 2731−2740

06CH11357, and the Canadian Light Source and its funding partners.

■ ABBREVIATIONS

LIB, lithium-ion battery; TM, transition metal; LNO, $LiNiO_2$; NMC, $LiNi_{1-x}(MnCo)_xO_2$; SE, super-exchange; HEXRD, high-energy X-ray diffraction; XAS, X-ray absorption spectroscopy; NPD, neutron powder diffraction; NMR, nuclear magnetic resonance; EXAFS, extended X-ray absorption fine structure; DOS, density of state; NMC712, $LiNi_{0.7}Mn_{0.1}Co_{0.2}O_2$; NMC721, $LiNi_{0.7}Mn_{0.2}Co_{0.1}O_2$; NMC71515, $LiNi_{0.7}Mn_{0.15}Co_{0.15}O_2$; NM73, $LiNi_{0.7}Mn_{0.3}O_2$; NC73, $LiNi_{0.7}Co_{0.3}O_2$; XANES, X-ray absorption near-edge structure

■ REFERENCES

(1) Rao, C. Transition Metal Oxides. *Annu. Rev. Phys. Chem.* **1989**, *40*, 291−326.

(2) Jung, S.-K.; Gwon, H.; Hong, J.; Park, K.-Y.; Seo, D.-H.; Kim, H.; Hyun, J.; Yang, W.; Kang, K. Understanding the Degradation Mechanisms of $LiNi_{0.5}Co_{0.2}Mn_{0.3}O_2$ Cathode Material in Lithium Ion Batteries. *Adv. Energy Mater.* **2014**, *4*, 1300787.

(3) Wu, Z.; Ji, S.; Zheng, J.; Hu, Z.; Xiao, S.; Wei, Y.; Zhuo, Z.; Lin, Y.; Yang, W.; Xu, K.; Amine, K.; Pan, F. Prelithiation Activates $Li(Ni_{0.5}Mn_{0.3}Co_{0.2})O_2$ for High Capacity and Excellent Cycling Stability. *Nano Lett.* **2015**, *15*, 5590−5596.

(4) Lim, B.-B.; Yoon, S.-J.; Park, K.-J.; Yoon, C. S.; Kim, S.-J.; Lee, J. J.; Sun, Y.-K. Advanced Concentration Gradient Cathode Materials with Two-Slope for High-Energy and Safe Lithium Batteries. *Adv. Funct. Mater.* **2015**, *25*, 4673−4680.

(5) Myung, S.-T.; Noh, H.-J.; Yoon, S.-J.; Lee, E.-J.; Sun, Y.-K. Progress in High-Capacity Core-Shell Cathode Materials for Rechargeable Lithium Batteries. *J. Phys. Chem. Lett.* **2014**, *5*, 671−679.

(6) Lu, J.; Chen, Z.; Ma, Z.; Pan, F.; Curtiss, L. A.; Amine, K. Role of Nanotechnology in Enabling High Power and High Energy Batteries Materials for Electric Vehicle Application. *Nat. Nanotechnol.* **2016**, *11*, 1031−1038.

(7) Whittingham, M. S. Ultimate Limits to Intercalation reaction for Lithium Batteries. *Chem. Rev.* **2014**, *114*, 11414−11443.

(8) Manthiram, A.; Knight, J. C.; Myung, S.-T.; Oh, S.-M.; Sun, Y.-K. Nickel-Rich and Lithium-Rich Layered Oxide Cathodes: Progress and Perspectives. *Adv. Energy Mater.* **2016**, *6*, 1501010.

(9) Liu, W.; Oh, P.; Liu, X.; Lee, M.-J.; Cho, W.; Chae, S.; Kim, Y.; Cho, J. Nickel-Rich Layered Lithium Transition-Metal Oxide for High-Energy Lihtium-Ion Batteries. *Angew. Chem., Int. Ed.* **2015**, *54*, 4440−4457.

(10) Rozier, P.; Tarascon, J. M. Li-Rich Layered Oxide Cathodes for Next-Generation Li-Ion Batteries: Chances and Challenges. *J. Electrochem. Soc.* **2015**, *162*, A2490−A2499.

(11) Manthiram, A.; Song, B.; Li, W. A Perspective on Nickel-Rich Layered Oxide cathodes for Lithium-Ion Batteries. *Energy Storage Mater* **2017**, *6*, 125−139.

(12) Kang, K.; Ceder, G. Factors That Affact Li Mobility in Layered Lithium Transition Metal Oxides. *Phys. Rev. B: Condens. Matter Mater. Phys.* **2006**, *74*, 094105.

(13) Lee, J.; Urban, A.; Li, X.; Su, D.; Hautier, G.; Ceder, G. Unlocking the Potential of Cation-Disordered Oxides for Rechargeable Lithium Batteries. *Science* **2014**, *343*, 519−522.

(14) Zheng, S.; Huang, R.; Makimura, Y.; Ukyo, Y.; Fisher, C. A. J.; Hirayama, T.; Ikuhara, Y. Microstructure Changes in $LiNi_{0.8}Co_{0.15}Al_{0.5}O_2$ Positive Electrode Material during the First Cycle. *J. Electrochem. Soc.* **2011**, *158*, A357−A362.

(15) Cui, S.; Wei, Y.; Liu, T.; Deng, W.; Hu, Z.; Su, Y.; Li, H.; Li, M.; Guo, H.; Duan, Y.; Wang, W.; Rao, M.; Zheng, J.; Wang, X.; Pan, F. Optimized Temperature Effect of Li-Ion Diffusion with Layer Distance in $Li(Ni_xMn_yCo_z)O_2$ Cathode Materials for High Performance Li-Ion Battery. *Adv. Energy Mater.* **2016**, *6*, 1501309.

(16) Zhang, M.-J.; Teng, G.; Chen-Wiegart, Y.-c. K.; Duan, Y.; Ko, J. Y. P.; Zheng, J.; Thieme, J.; Dooryhee, E.; Chen, Z.; Bai, J.; Amine, K.; Pan, F.; Wang, F. Cationic Ordering Coupled to Reconstruction of Basic Building Units during Synthesis of High-Ni Layered Oxides. *J. Am. Chem. Soc.* **2018**, *140*, 12484−12492.

(17) Wang, D.; Kou, R.; Ren, Y.; Sun, C.-J.; Zhao, H.; Zhang, M.-J.; Li, Y.; Huq, A.; Ko, J. Y. P.; Pan, F.; Sun, Y.-K.; Yang, Y.; Amine, K.; Bai, J.; Chen, Z.; Wang, F. Synthetic Control of Kinetic Reaction Pathway and Cationic Ordering in High-Ni Layered Oxide Cathodes. *Adv. Mater.* **2017**, *29*, 1606715.

(18) Li, Y.; Xu, R.; Ren, Y.; Lu, J.; Wu, H.; Wang, L.; Miller, D. J.; Sun, Y.-K.; Amine, K.; Chen, Z. Synthesis of Full Concentration Gradient Cathode Studied by High Energy X-Ray Diffraction. *Nano Energy* **2016**, *19*, 522−531.

(19) Wei, Y.; Zheng, J.; Cui, S.; Song, X.; Su, Y.; Deng, W.; Wu, Z.; Wang, X.; Wang, W.; Rao, M.; Lin, Y.; Wang, C.; Amine, K.; Pan, F. Kinetics Tuning of Li-Ion Diffusion in Layered $Li(Ni_xMn_yCo_z)O_2$. *J. Am. Chem. Soc.* **2015**, *137*, 8364−8367.

(20) Van der Ven, A.; Ceder, G. Lithium Diffusion in Li_xCoO_2. *Electrochem. Solid-State Lett.* **1999**, *3*, 301−304.

(21) Reed, J.; Ceder, G. Charge, Potential, and Phase Stability of Layered $Li(Ni_{0.5}Mn_{0.5})O_2$. *Electrochem. Solid-State Lett.* **2002**, *5*, A145−A148.

(22) Reed, J.; Ceder, G. Role of Electronic Structure in the Subsceptibility of Metastable Transition-Metal Oxide Strucures to Transformation. *Chem. Rev.* **2004**, *104*, 4513−4534.

(23) Kim, Y.; Kim, D.; Kang, S. Experimental and First-Principles Thermodynamic Study of the Formaiton and Effects of Vacancies in Layered Lithiumm Nickel Cobalt Oxides. *Chem. Mater.* **2011**, *23*, 5388−5397.

(24) Ellis, B. L.; Lee, K. T.; Nazar, L. F. Positive Electrode Materials for Li-Ion and Li-Batteries. *Chem. Mater.* **2010**, *22*, 691−714.

(25) Kramers, H. A. interaction Entre les Atomes Magnétogènes dans un Cristal Paramagnétique. *Physica* **1934**, *1*, 182−192.

(26) Chen, H.; Dawson, J. A.; Harding, J. H. Effects of Cationic Substitution on Structural Deffects in Layered Cathode Materials $LiNiO_2$. *J. Mater. Chem. A* **2014**, *2*, 7988−7996.

(27) Wannier, G. H. Antiferromagnetism. The Triangular Ising Net. *Phys. Rev.* **1950**, *79*, 357−364.

(28) Lacroix, C.; Mendels, P.; Mila, F. *Introduction to Frustrated Magnetism: Materials, Experiments, Theory*; Springer: Heidelberg, Germany, 2011.

(29) Taguchi, Y.; Oohara, Y.; Yoshizawa, H.; Nagaosa, N.; Tokura, Y. Spin Chirality, Berry Phase, and Anormalous Hall Effect in a Frustrated Ferromagnet. *Science* **2001**, *291*, 2573−2576.

(30) Xiao, Y.; Liu, T.; Liu, J.; He, L.; Chen, J.; Zhang, J.; Luo, P.; Lu, H.; Wang, R.; Zhu, W.; Hu, Z.; Teng, G.; Xin, C.; Zheng, J.; Liang, T.; Wang, F.; Chen, Y.; Huang, Q.; Pan, F.; Chen, H. Insight into the Origin of Lithium/Nickel Ions Exchange in Layered $Li(Ni_xMn_yCo_z)O_2$ Cathode Materials. *Nano Energy* **2018**, *49*, 77−85.

(31) Lee, W.; Muhammad, S.; Kim, T.; Kim, H.; Lee, E.; Jeong, M.; Son, S.; Ryou, J.-H.; Yoon, W.-S. Rechargeable Batteries: New Insight into Ni-Rich Layered Structure for Next-Generation Li Rechargeable Batteries. *Adv. Energy Mater.* **2018**, *8*, 1701788.

(32) Zhao, J.; Zhang, W.; Huq, A.; Misture, S. T.; Zhang, B.; Guo, S.; Wu, L.; Zhu, Y.; Chen, Z.; Amine, K.; Pan, F.; Bai, J.; Wang, F. In-situ Probing and Synthetic Control of Cationic Ordering in Ni-rich Layered Oxide Cathodes. *Adv. Energy Mater.* **2017**, *7*, 1601266.

(33) Sata, T. High-Temperature Vaporization of Li_2O Component from Solid Solution $Li_xNi_{1-x}O_2$ in Air. *Ceram. Int.* **1998**, *24*, 53−59.

(34) Yoon, W.-S.; Iannopollo, S.; Grey, C. P.; Carlier, D.; Gorman, J.; Reed, J.; Ceder, G. Local Structure and Cation Ordering in O3 Lithium Nickel Manganese Oxides with Stoichiometry $Li[Ni_xMn_{(2-x)/3}Li_{(1-2x)/2}]O_2$: NMR Studies and First Principles Calculations. *Electrochem. Solid-State Lett.* **2004**, *7*, A167−A171.

(35) Xu, G.-L.; Amine, R.; Xu, Y.-F.; Liu, J.; Gim, J.; Ma, T.; Ren, Y.; Sun, C.-J.; Liu, Y.; Zhang, X.; Heald, S. M.; Solhy, A.; Saadoune, I.;

DOI: 10.1021/acs.chemmater.8b04673
Chem. Mater. 2019, 31, 2731−2740

Mattis, W. L.; Sun, S.-G.; Chen, Z.; Amine, K. Insights into the structure effects of Layered Cathode Materials for High Voltage Sodium-Ion Batteries. *Energy Environ. Sci.* **2017**, *10*, 1677−1693.
(36) Rougier, A.; Delmas, C.; Chadwick, A. V.; Chadwick, A. V. Non-Cooperative Jahn-Teller Effect in $LiNiO_2$: A XAFS Study. *Solid State Commun.* **1995**, *94*, 123−127.
(37) Balasubramanian, M.; Sun, X.; Yang, X. Q.; McBreen, J. In-Situ X-Ray Absorption Studies of a High-Rate $LiNi_{0.85}Co_{0.15}O_2$ Cathode Material. *J. Electrochem. Soc.* **2000**, *147*, 2903−2909.
(38) Ohzuku, T.; Makimura, Y. Formation of Solid Solution and Its Effect on Lithium Insertion Schemes for Advanced Lithiun-Ion Batteries: X-Ray Absorption Spectroscopy and X-Ray Diffraction of $LiCoO_2$, $LiCo_{1/2}Ni_{1/2}O_2$ and $LiNiO_2$. *Res. Chem. Intermed.* **2006**, *32*, 507−521.
(39) Tsai, Y. W.; Hwang, B. J.; Ceder, G.; Sheu, H. S.; Liu, D. G.; Lee, J. F. In-Situ X-Ray Absorption Spectroscopy Study on Variation of Electronic Transitions and Local Structure of $LiNi_{1/3}Co_{1/3}Mn_{1/3}O_2$ Cathode Material during Electrochemical Cycling. *Chem. Mater.* **2005**, *17*, 3191−3199.
(40) Liu, X.; Weng, T.-C. Synchrotron-Based X-Ray Absorption Spectroscopy for Energy Materials. *MRS Bull.* **2016**, *41*, 466−472.
(41) Delmas, C.; Ménétrier, M.; Croguennec, L.; Saadoune, I.; Rougier, A.; Pouillerie, C.; Prado, G.; Grüne, M.; Fournès, L. An Overview of the $Li(Ni,M)O_2$ systems: Syntheses, Structures and Properties. *Electrochim. Acta* **1999**, *45*, 243−253.
(42) Kanamori, J. Superexchange Interaction and Symmetry Properties of Electron Obitals. *J. Phys. Chem. Solids* **1959**, *10*, 87−98.
(43) Whittingham, M. S. Lithium Batteries and Cathode Materials. *Chem. Rev.* **2004**, *104*, 4271−4302.
(44) Mohan, P.; Kumar, K. A.; Kalaignan, G. P.; Muralidharan, V. S. Improved Electrochemical Properties of Chromium Substituted in $LiCr_{1-x}Ni_xO_2$ Cathode Materials for Rechargeable Lihtium-Ion Battereis. *J. Solid State Electrochem.* **2012**, *16*, 3695−3702.

DOI: 10.1021/acs.chemmater.8b04673
Chem. Mater. 2019, 31, 2731−2740